Active Remote Sensing of Snow Using NMM3D/DMRT and Comparison With CLPX II Airborne Data

Xiaolan Xu, *Student Member, IEEE*, Ding Liang, Leung Tsang, *Fellow, IEEE*, Konstantinos M. Andreadis, Edward G. Josberger, Dennis P. Lettenmaier, Donald W. Cline, and Simon H. Yueh, *Fellow, IEEE*

***Abstract*—We applied the Numerical Maxwell Model of three-dimensional simulations (NMM3D) in the Dense Media Radiative Theory (DMRT) to calculate backscattering coefficients. The particles' positions are computer-generated and the subsequent Foldy-Lax equations solved numerically. The phase matrix in NMM3D has significant cross-polarization, particularly when the particles are densely packed. The NMM3D model is combined with DMRT in calculating the microwave scattering by dry snow. The NMM3D/DMRT equations are solved by an iterative solution up to the second order in the case of small to moderate optical thickness. The numerical results of NMM3D/DMRT are illustrated and compared with QCA/DMRT. The QCA/DMRT and NMM3D/DMRT results are also applied to compare with data from two specific datasets from the second Cold Land Processes Experiment (CLPX II) in Alaska and Colorado. The data are obtained at the Ku-band (13.95 GHz) observations using airborne imaging polarimetric scatterometer (POLSCAT). It is shown that the model predictions agree with the field measurements for both co-polarization and cross-polarization. For the Alaska region, the average snow depth and snow density are used as the inputs for DMRT. The grain size, selected from within the range of the ground measurements, is used as a best-fit parameter within the range. For the Colorado region, we use the Variable Infiltration Capacity Model (VIC) to obtain the input snow profiles for NMM3D/DMRT.**

***Index Terms*—CLPX, dense media radiative transfer, numerical Maxwell model, QCA, snow, VIC.**

I. Introduction

THE Snow and Cold Land Process (SCLP) satellite mission has been recommended by the 2007 Decadal Study of the Committee on earth Science and Applications. Careful studies of airborne datasets and ground-based measurements are important for feasibility studies of the satellite mission. The SCLP mission will combine active and passive microwave sensors. Using the same forward physical model in both active and passive microwave remote sensing is useful in understanding the scattering properties of snow [1]. It is also important to show that the microwave signatures of active and passive microwave remote sensing are consistent. The satellite-borne microwave radiometer Advanced Microwave Scanning Radiometer—EOS (AMSR-E) has coarse resolution and the measurement of a single pixel arises from contributions of a variety of complex land cover. High-resolution active radar provides detailed spatial studies of the inhomogeneous landscapes. In addition to SCLP, Cold Regions Hydrology High-resolution Observatory (CoReH2O) was selected by the European Space Agency (ESA) for detailed feasibility studies (Phase A) that commenced in mid2009. Both the SCLP and CoReH2O satellite missions include dual-frequency synthetic aperture radar [2].

Previously, we have used Quasi-Crystalline Approximation applied in Dense Media Radiative Theory (QCA/DMRT) model for both active and passive remote sensing [3]. The sticky particle model was used. It is shown that with one set of physical parameters, the multi-layer dense media transfer theory model can simultaneously match four channels (vertical and horizontal polarization of Ku- and Ka-band) of ground-based brightness temperature measurements in CLPX-I [2]. When applying QCA/DMRT to active remote sensing, the simulation results of co-polarization vv and hh backscattering agree with the measurements, but the cross-polarization (vh/hv) is usually underestimated. It is to be noted that QCA consists of single scattering of the coherent field. Thus, QCA does not contain cross-polarization in the phase matrix as exhibited in the 1–2 frame. The cross-polarization backscattering of QCA/DMRT arises from the second-order solution of DMRT that contains the product of phase matrices. However, the measurements data show strong cross-polarization response in the middle of winter. To explain the strong cross-polarization backscattering in the measurement data, we have applied Numerical Maxwell Method of 3-Dimensional (NMM3D) simulations to calculate the phase matrices and extinction coefficients. The snow microstructure is represented by clusters of spheres, the positions of which are computer-generated. The spheres are placed randomly in a box. Bonding is allowed between the spheres to simulate the ice grain cluster structure in snow [5]. The rigorous solutions of Maxwell Equations in the form

Manuscript received March 15, 2010; revised May 12, 2010; accepted June 11, 2010. Date of publication August 16, 2010; date of current version December 15, 2010. This work was supported in part by the National Aeronautics and Space Administration.

X. Xu, D. Liang, and L. Tsang are with the Electrical Engineering Department, University of Washington, Seattle, WA 98195 USA (e-mail: xlxu@uw.edu).

K. M. Andreadis and D. P. Lettenmaier are with the Department of Civil and Environmental Engineering, University of Washington, Seattle, WA 98195 USA.

E. G. Josberger is with the U.S. Geological Survey, Washington Water Science Center, Tacoma, WA 98402 USA.

D. W. Cline is with the National Operational Hydrologic Remote Sensing Center, NOAA, Chanhassen, MN 55317 USA.

S. H. Yueh is with the Jet Propulsion Laboratory, California Institute of Technology, Pasadena, CA 91109 USA.

Color versions of one or more of the figures in this paper are available online at http://ieeexplore.ieee.org.

Digital Object Identifier 10.1109/JSTARS.2010.2053919

of Foldy-Lax multiple scattering equations are solved. The coherent wave interactions between the particles that are within wavelengths from each other are accounted for so that the phase matrix exhibits cross-polarization, particularly when the particles are densely packed. The non-zero cross-polarization phase matrix gives larger cross-polarization backscattering coefficients. In a previous paper [6], NMM3D only used to simulate co-polarization and cross-polarization phase matrices.

In this paper, we combine the Numerical Maxwell Model of three-dimensional simulations (NMM3D) with the Dense Media Radiative Theory (DMRT) to calculate backscattering coefficients in microwave active remote sensing of snow structures. The NMM3D/DMRT equations were solved by iterative solution up to the second order. The numerical results of NMM3D/DMRT were illustrated and compared with QCA/DMRT [7]. Then, the models of both NMM3D/DMRT and QCA/DMRT were applied to compare with airborne data in CLPX II. CLPX II datasets were collected by NASA Jet Propulsion Laboratory (JPL) POLSCAT radar, which has four channels (VV HH HV VH) at Ku-band with the center frequency at 13.95 GHz. The simulations in this paper are calculated at this frequency.

The CLPX II experiments were completed in Alaska and Colorado during 2006–2008 winters [8]. In Alaska region, there were two field campaigns flown during the winter of 2007–2008. The *in situ* ground observations were also sampled at the same time. The *in situ* ground observations indicated that there was no forest cover in the field campaigns. Short grasses were embedded in the snow in some places. We assume that the short grass scattering is negligible so that the DMRT model of dry snow can be applied. We selected the POLSCAT pixels where the ground measurements were also available. In one pixel, several measurement samples were collected. We used the average of these measurement samples to obtain the snow density and snow depth in the model simulations. As for the grain size, it was selected from within the range of the ground measurements. Within this range, it is used as a best-fit parameter. The results showed that QCA/DMRT simulations have good agreements with the co-polarization backscattering and NMM3D/DMRT simulations have good agreements with both the cross-polarization and the co-polarization measurements.

The flights over Colorado region were collected during Dec. 2006 to Mar. 2008. As *in situ* measurements are not available in Colorado region, we use the snow hydrology Variable Infiltration Capacity (VIC) [9] model to generate the snow properties and couple these properties with Dense Media Radiative Transfer (DMRT) models. VIC is a macroscale hydrology model that solves the energy and water balance over a gridded domain. It provides snow properties which are then used as the inputs for the DMRT model. We tested the coupled-model in the Lake Catamount region, which is covered by snow during the winter. It is shown that the model predictions agree with the observations. In the flight campaigns, parts of the flights are over the coniferous, deciduous forests and sagebrush cover. As this paper is focused on the snow model, we chose only the POLSCAT data over forest-free areas.

In Section II, we provide the theoretical formulations of NMM3D/DMRT. The NMM3D/DMRT results are illustrated and compared with QCA/DMRT. The hydrology model VIC is described in Section III. In Section IV, we show the data comparison results at Alaska and Colorado. Conclusions are drawn in Section V.

II. NMM3D/DMRT Formulation

Snow is a random medium with interesting microstructure morphologies [10], [11]. To describe the snow structure, we model the dry snow packs as consisting of densely packed spheres. The spheres can bond to each other through adhesive forces to form aggregates. For scattering by a collection of spheres, multiple scattering can be formulated by Foldy-Lax equations. The Foldy-Lax equations are derived from Maxwell equations [12]. In Foldy-Lax equations, we first expand the plane incident wave $\overline{E}^{\rm inc}(\overline{r})$ into a summation of the vector spherical waves

$$\overline{E}^{\rm inc}(\overline{r})=\sum_{m,n}\left[a_{mn}^{(M)}Rg\overline{M}_{mn}(kr,\theta,\phi)+a_{mn}^{(N)}Rg\overline{N}_{mn}(kr,\theta,\phi)\right]. \tag{1}$$

Then the field of the excitation wave on a particle can be written in the similar form

$$\overline{E}_l^{ex}(\overline{r})=\sum_{mn}\left[w_{mn}^{(M)(l)}Rg\overline{M}_{mn}(k\overline{rr_l})+w_{mn}^{(N)(l)}Rg\overline{N}_{mn}(k\overline{rr_l})\right]. \tag{2}$$

The Foldy-Lax equations state that the field exciting a particle is the sum of incident wave and scattered wave from all other scatterers.

$$\overline{E}_l^{ex}=\overline{E}^{\rm inc}+\overline{\overline{G}}_0\sum_{j=1,j\neq l}^{N}\overline{\overline{T}}_j\overline{E}_j^{ex} \tag{3}$$

A set of linear equations can be derived for $w_{mn}^{(M)(l)}$ and $w_{mn}^{(N)(l)}$ by substituting (1) and (2) into (3).

$$\overline{w}^{(q)}=\sum_{p=1,p\neq q}^{N}\overline{\overline{\sigma}}(k\overline{r_qr_p})\overline{\overline{T}}^{(p)}\overline{w}^{(p)}+e^{i(\overline{k_i}\bullet\overline{r_q})}\overline{a}_{\rm inc} \tag{4}$$

The matrix equations in (4) of Foldy-Lax are solved numerically. The advantage of Foldy-Lax equations is that the vector spherical waves are used as basis functions rather than fine discretization of each particle in the Method of Moment (MoM) or Finite Difference Time Domain method (FDTD) or Finite Element Method (FEM). Thus, this method has significantly fewer unknowns than the other methods. Detailed formula can be found in [6]. In computer generation of sphere positions, we allow up to three particles simultaneously bonding with each others. Successive bondings result in aggregates. We use shuffling method to generate different realizations of the particle positions. For each realization, the Foldy-Lax equations are solved. The computed scattered field is decomposed into coherent field, which is the average field and the incoherent field. As the particles are placed randomly, the phase of the scattered field in all directions will fluctuate except in the forward direction. In the forward direction, the scattered waves of each particle are in phase, which contribute to the coherent wave. However, the coherent forward scattering does not contribute to the phase matrix nor the scattering coefficient. We subtract

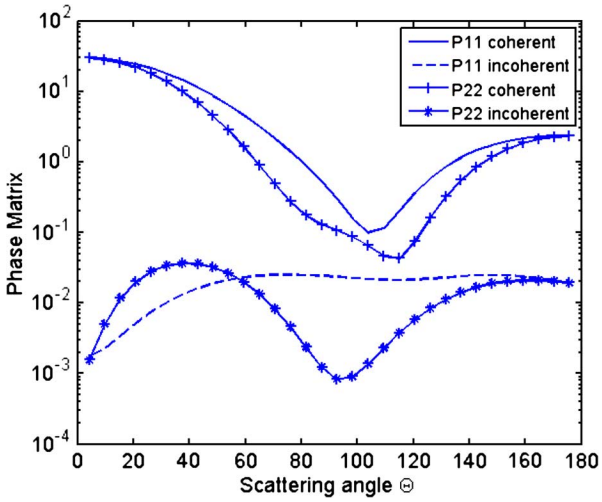

Fig. 1. Incoherent phase matrix and coherent phase matrix comparison. $\mathrm{Fv} = 30\%$, $\mathrm{diameter} = 1$ mm. Cubic box with side $\mathrm{L} = 0.7$ wavelength.

the coherent wave from the total scattered field to obtain the incoherent field. The coherent scattered wave is calculated by averaging the scattering waves over realizations.

$$\left\langle \overline{E}_s(\theta_s,\phi_s)\right\rangle = \frac{1}{N_r}\sum_{i=1}^{N_r}\overline{E_s^i}(\theta_s,\phi_s) \tag{5}$$

The incoherent wave is

$$\widetilde{E}_s^i(\theta_s,\phi_s) = \overline{E}_s^i(\theta_s,\phi_s) - \left\langle \overline{E}_s(\theta_s,\phi_s)\right\rangle \tag{6}$$

where i is the realization index, N_r is the total number of realizations. Then, the phase matrix of DMRT is calculated from the bistatic scattering properties of the incoherent scattering wave intensity. The results of the computed phase matrix are conveniently illustrated in the 1–2 frame polarization coordinate system [13].

$$\begin{bmatrix} \left\langle |\widetilde{E}_{1s}|^2\right\rangle \\ \left\langle |\widetilde{E}_{2s}|^2\right\rangle \end{bmatrix} = \begin{bmatrix} P_{11} & P_{12} \\ P_{21} & P_{22} \end{bmatrix} \begin{bmatrix} |\overline{E}_{1i}|^2 \\ |\overline{E}_{2i}|^2 \end{bmatrix} \tag{7}$$

In Fig. 1, we plot the incoherent phase matrix compared with coherent phase matrix. The coherent phase matrix is mostly in the forward direction because of the finite box size. The magnitudes and angular distribution of the coherent phase matrix are related to the shape and size of the sample box in which the particles are placed. For an infinite box size, the coherent wave will be a delta function in the forward direction. The magnitudes of incoherent phase matrix are smaller than the coherent phase matrix and its magnitudes and angular distributions are not dependent on the shape and size of the sample box. In the limit of sparse concentration of particles, the computed phase matrix of the incoherent wave agrees with that used in conventional radiative transfer theory of independent scattering.

In microwave active remote sensing of snow, the cross-polarization in the phase matrix traditionally has been attributed to arise from scattering by the non-spherical particles [14], [15]. For example, when the incident wave is impinging on an ellipsoid particle, the tangential component of the incident field

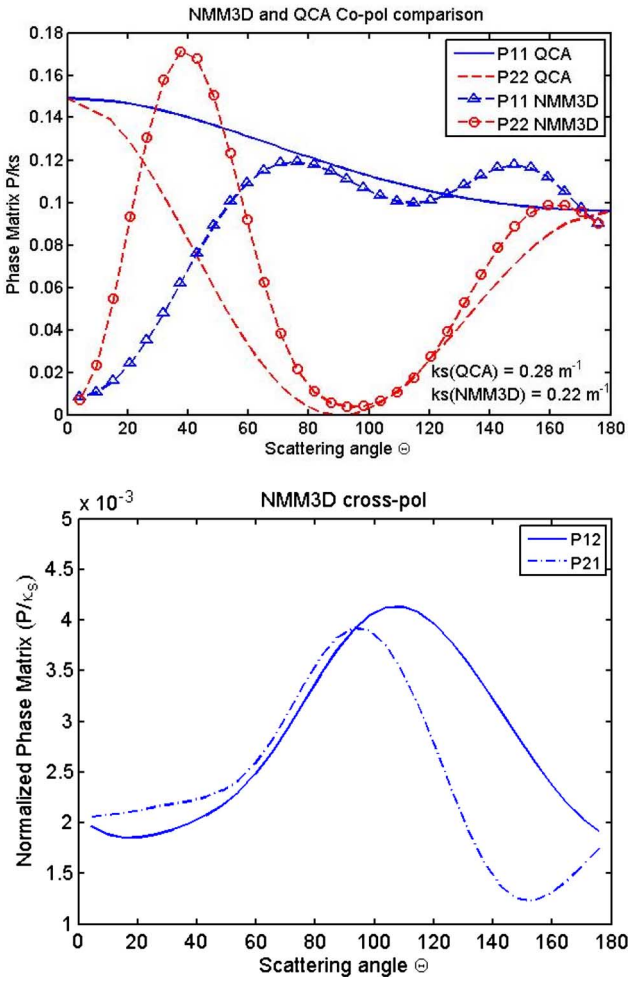

Fig. 2. Phase matrix comparison between QCA and NMM3D at $\mathrm{fv} = 30\%$, $\mathrm{diameter} = 1$ mm. Co-polarization comparison (Top). Cross-polarization comparison (Bottom).

can better penetrate into the particles while the normal component is decreased by the relative permittivity. In that case, the induced dipole inside the ellipsoid is not aligned with the incident electric field. In the NMM3D model, we offer a different physical model and still use spheres. We allow the spheres to adhere to each other to simulate the nonsymmetrical aggregate structure of snow. We then solve the wave interactions among particle aggregates. Since the spheres are very close to each other in the wavelength scale, the near-field coherent interactions of the spheres are significant. The electric dipole of each sphere is strongly influenced by the dipoles of neighborhood spheres and will no longer align in the same direction as the electric field of the incident wave. Thus, the non-zero cross-polarization appears in the phase matrix which is clearly exhibited in the 1–2 polarization frame. This results in strong cross-polarization backscattering. The cross-polarization calculated by NMM3D is shown in Fig. 2 (Bottom).

In Fig. 2, we also show the co-polarization phase matrices compared with Quasi-Crystalline Approximation (QCA). The NMM3D results exhibit similar trend as that of QCA. The backward scattering is from 90 to 180 degree, and the forward scattering is from 0 to 90 degree. The phase matrices between

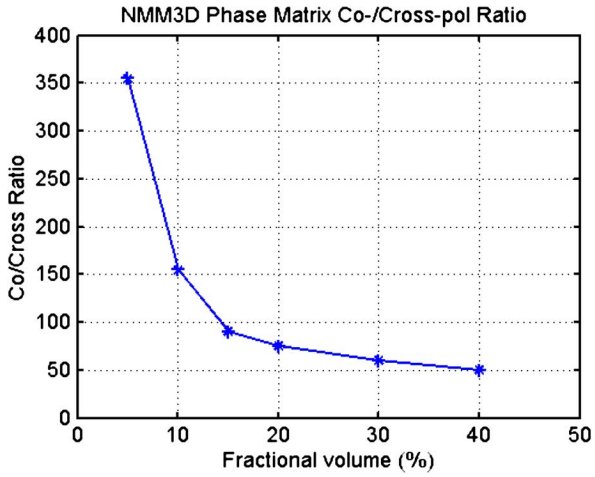

Fig. 3. Co-pol to cross-pol ratio changes with fractional volume grain size = 1 mm at 14 GHz.

NMM3D and QCA agree in the backward direction. In the forward direction of NMM3D, the forward coherent field has been subtracted. Therefore, at 0 degree, the NMM3D phase matrices decrease to zero.

In Fig. 3, we show the ratio of co-polarization to cross-polarization versus the fractional volume. The ratio decreases with the increase in fractional volume. The fractional volume is calculated as follows,

$$fv = \frac{\rho_{snow}}{\rho_{ice}} \tag{8}$$

where ρ_{ice} is the ice density and ρ_{snow} is the snow density. Fig. 3 also shows that the cross polarization increases with snow density in the NMM3D model.

The datasets in the Colorado region reveal that from January to February 2007, the HV backscattering increased more rapidly than VV backscattering. As we show in Fig. 3, the cross-polarization backscattering is more sensitive to the snow density. Thus, the rapidly increasing cross-polarization may reflect the density change in the snow pack during the winter. In addition, we examine the frequency dependence of the NMM3D results of extinction coefficients, which is about 2.5 to 2.8 for the sticky case. The results are consistent with experiment measurements [16], [17].

Next, we substitute the NMM3D results of extinction and phase matrix into the dense media radiative transfer equation. The DMRT equation is

$$\frac{d\overline{I}(\overline{r},\hat{s})}{ds} = -\kappa_e \overline{I}(\overline{r},\hat{s}) + \int_{4\pi} d\Omega' \overline{\overline{P}}(\overline{r},\hat{s},\hat{s}') \cdot \overline{I}(\overline{r},\hat{s}') \tag{9}$$

where $\overline{I}$ is the specific intensity, κ_e is extinction coefficient and $\overline{\overline{P}}$ is the phase matrix in the principal frame. Previously, the 1–2 frame is used in the phase matrices calculation of NMM3D. We transform the phase matrix from the 1–2 frame to the principal frame through transformation matrix. The extinction coefficient can be calculated by

$$\kappa_e = \kappa_a + \kappa_s \tag{10}$$

where κ_a is absorption coefficient. The absorption coefficient is calculated from the internal electric fields of the particles. The scattering coefficient κ_s is calculated by the integration of the phase matrix elements in the 1–2 frame as follows

$$\kappa_s = \pi \int_0^{\pi} d\Theta \left(P_{11}(\Theta) + P_{22}(\Theta) + P_{12}(\Theta) + P_{21}(\Theta)\right) \sin(\Theta) \tag{11}$$

We used iterative method to solve the DMRT equations up to the second order. The iterative method assumes that the phase matrix is a small parameter. The explicit second order analytical solutions can be found in [13]. There are four terms in the first-order solution, all related to the phase matrix directly. The second-order solution requires a solid angle integration of the intermediate directions in the product of phase matrices. Because of the non-zero cross-polarization in the NMM3D phase matrix, the first-order solution of NMM3D/DMRT contributes to the cross-polarization of the backscattering, unlike classical Mie scattering and QCA/DMRT. Thus, the cross polarization of NMM3D/DMRT arises from 1) the phase matrix in the first order solution and 2) the product of phase matrices in the second order solution.

In Fig. 4, we plot the bistatic scattering VV, HH, HV, and VH of first- and second-order solution for a snow depth of 30 cm. The incident angle is 35 degree, which is the same as in the POLSCAT datasets. The grain size is 1 mm diameter and the fractional volume is 40%. The optical thickness in this case is 0.06, and the albedo is 0.9. In the first-order solution, the NMM3D/DMRT gives fairly large cross-polarization backscattering. The backscattering angle is denoted by a negative angle at -35 degree. In Fig. 4, we also present the second-order result (the sum of the first-order solution and the second-order solution) of the NMM3D/DMRT. The cross-polarization is merely 6 dB lower than the co-polarization and 8 dB larger than the first solution in the backscattering direction. The second-order bistatic scattering between the QCA/DMRT and NMM3D/DMRT are compared in Fig. 5. The snow parameters are fv $= 30\%$, and the grain size $= 1$ mm. The co-polarization results of NMM3D/DMRT and QCA/DMRT are comparable. However, NMM3D/DMRT predicts more than 2 dB higher cross-polarization in the backscattering direction than QCA/DMRT.

In Fig. 6, we plot the backscattering coefficient as a function of snow depth. Both the first-order solution and the second-order results are shown. The co-polarization components in the first- and second-order solutions are comparable and are dependent on snow depth. The cross-polarization in the second-order solution is larger than in the first-order solution and more sensitive to changes in the snow depth. In Fig. 7, two different grain sizes are used. The backscattering coefficients at both grain sizes show strong dependence on the snow depth. The magnitude differences between the co-polarization and cross-polarization decrease with the increase in grain size.

III. Hydrology Model (VIC) Used in Colorado

As mentioned earlier, we use the ground measurements as the input to DMRT for the Alaska region measurements. For

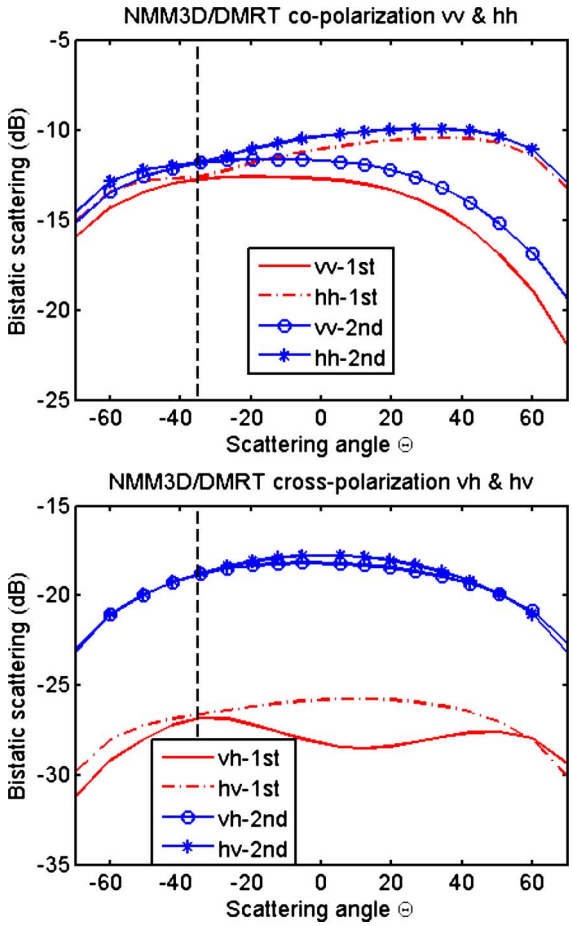

Fig. 4. Bistatic scattering coefficient of 1st and 2nd order solution with grain size = 1 mm, fractional volume = 40%, snow depth = 30 cm. Co-polarization Comparison (vv and hh) (Top). Cross-polarization (vh and hv) (Bottom).

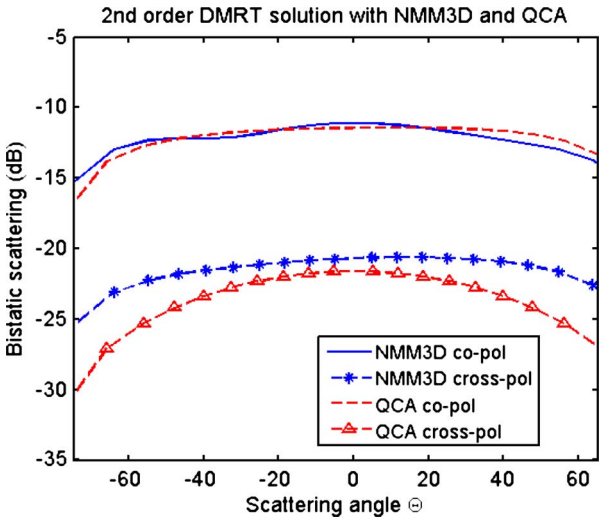

Fig. 5. Bisctatic scattering comparison between 2nd order NMM3D/DMRT and QCA/DMRT.

the Colorado measurements, there were no ground measurement data. In this case, we used the outputs computed by the Hydrology VIC model. VIC is a macroscale hydrology model that solves the energy and water balance over a gridded domain

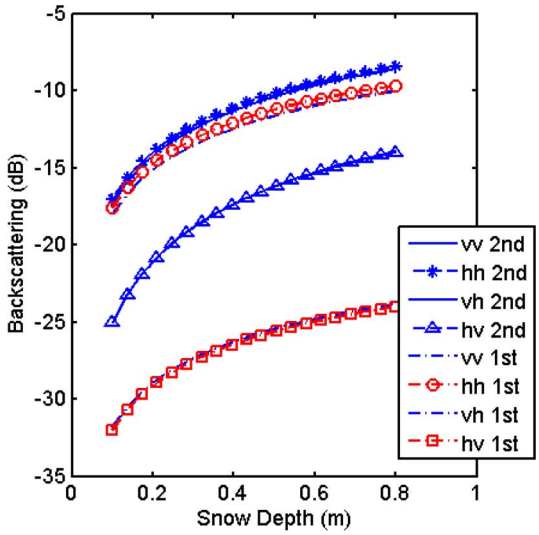

Fig. 6. Backscattering coefficient as a function of snow depth. Grain size = 1 mm.

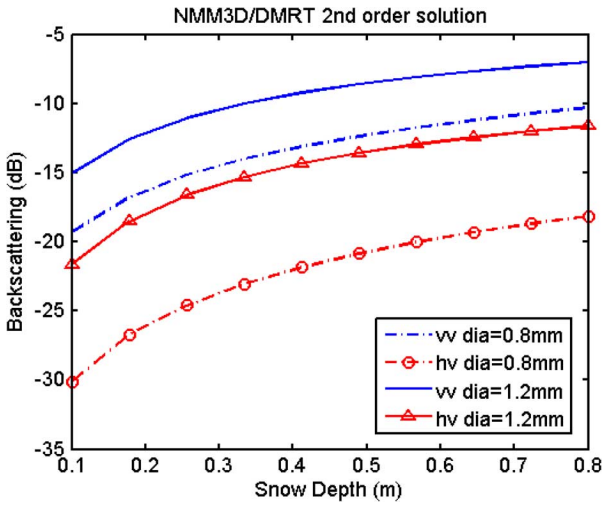

Fig. 7. Backscattering coefficients as a function of snow depth with different grain size.

[18]. The major difference compared with other land surface models is the parameterization of the subgrid variability of soil moisture, precipitation, topography, and vegetation. Each model grid cell can have multiple soil layers and is partitioned into tiles of different vegetation types and elevation zones. Moisture and energy fluxes are computed separately for each vegetation class and elevation band within each grid cell and then area-weighted and summed over the grid cell.

Snow accumulation and ablation processes are simulated using a two-layer energy and mass balance approach [19], [20]. The snowpack is allowed to exchange heat with the atmosphere through the surface layer, while the bottom layer acts a reservoir for the excess snow mass from the surface layer. The model simulates the effects of canopies on snow processes through interception, drip, mass release and through fall. Melting/refreezing is accounted for within each layer, while water percolation is simulated based on a preset liquid water holding capacity. Snow densification and grain growth

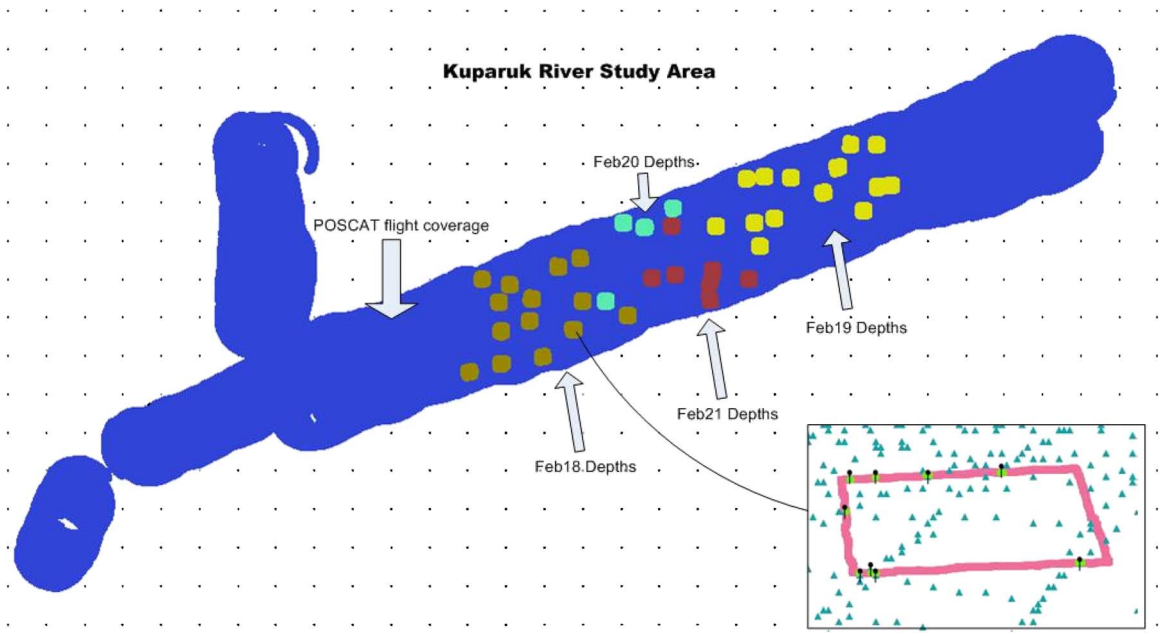

Fig. 8. Kuparuk River depth transects and snow pits.

algorithms have been adapted from the 1-D detailed snow physics model SNTHERM. Additionally, VIC can also simulate frozen soils as well as heat conduction between the pack and the soil layer.

The minimum requirements for VIC meteorological data include daily precipitation and minimum and maximum air temperature and wind speed. The model can disaggregate them and internally estimate other meteorological forcing variables such as downward solar radiation and relative humidity at the hourly time step. VIC simulations over the Colorado study area were performed at an hourly time step and a spatial resolution of 1 km. Topographic information was derived from the GTOPO30 digital elevation model (DEM), while the land cover for each pixel was derived from the 1-km Advanced Very High Resolution Radiometer (AVHRR) global land-cover dataset using the University of Maryland classification. Precipitation and air temperature data were obtained by a spatial interpolation of National Oceanic and Atmospheric Administration (NOAA) Cooperative Observer data using the synergraphic mapping system algorithm (SYMAP) and were gridded to the desired spatial resolution. The interpolated data were rescaled at the 4-km spatial resolution to match the Parameter-Elevation Regressions on Independent Slopes (PRISM) monthly precipitation and maximum and minimum temperature products [21] before being gridded to the 1-km resolution. The aforementioned approach allows for the simulation of snow water equivalent, depth, density, grain size, temperature, and ground temperature over the Colorado study area at a 1-km spatial resolution, from 10/1/2007 to 2/29/2008. The Land Data Assimilation System is used to calibrate model parameters [22].

IV. Model Comparisons With CLPX II Data

The datasets were collected by JPL POLSCAT radar as part of the second Cold Land Processes Field Experiment (CLPX II). The purposes of CLPX II were to advance airborne and spaceborne snow measurements and to enable the development of a retrieval algorithm for snow water equivalent (SWE). A physical-based forward model is important to understand the radar sensitivity to the key properties of the snowpack.

POLSCAT is a Ku-band polarimetric scatterometer operating at 13.95 GHz. It can record four channel (VV, HH, VH, HV) radar responses simultaneously. The POLSCAT radar was installed on a Twin Otter aircraft and operated at a 35-degree incident angle. In winter from 2006–2008, over twenty flights were flown over the Rocky Mountains in Colorado and the North Slope of Alaska.

A. Alaska Region

The field campaigns in Alaska were conducted on the North Slope of the Brooks Range, approximately 450 km north of Fairbanks. There were two Intense Study Areas (ISA), the Kuparuk (Kup) River and the Sagavanirktok (Sag) River, and two Intense Observation Periods (IOP): November 28 to December 3, 2007 (IOP1) and February 18–24, 2008 (IOP2). To ensure the snow cover, we chose the data from IOP2. The data we chose are from the Kuparuk River in February of 2008.

The snow properties for input in DMRT models are snow depth, snow density, and grain size. The footprint of the POLSCAT is 100 m, and the depth samples include several 200 m $\times$ 200 m square area in the flight coverage, as shown in Fig. 9.

For each snowpit, the SWE and grain size were sampled at each corner of the square. The data used in the model were from the points where the ground measurement and the center of the flight footprint coincide, as marked in the subplot of Fig. 8. The input snow depth and snow density for the model are the average of the four corner measurements. The grain sizes in the DMRT model are selected from the range of measurements, and are treated as best-fit parameters within the measurement range.

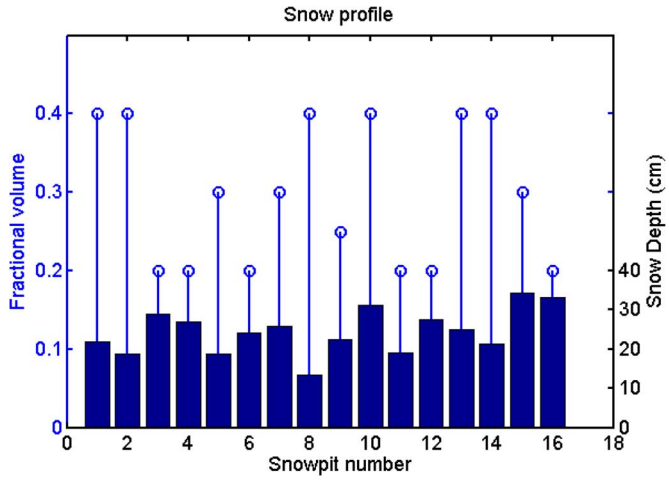

Fig. 9. Snow depth and fractional volume in different snowpit.

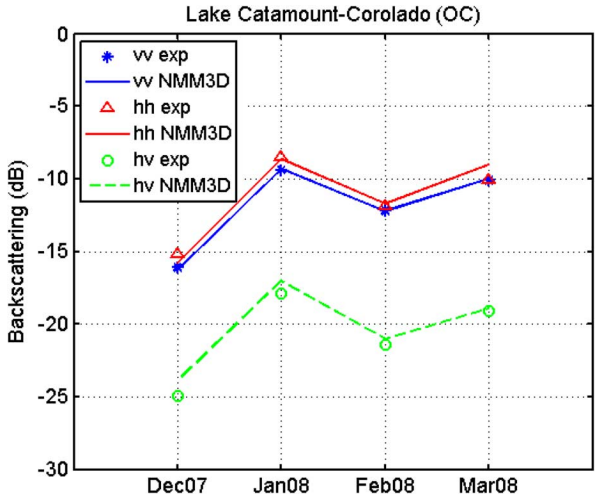

Fig. 11. Time series data match at Lake Catamount.

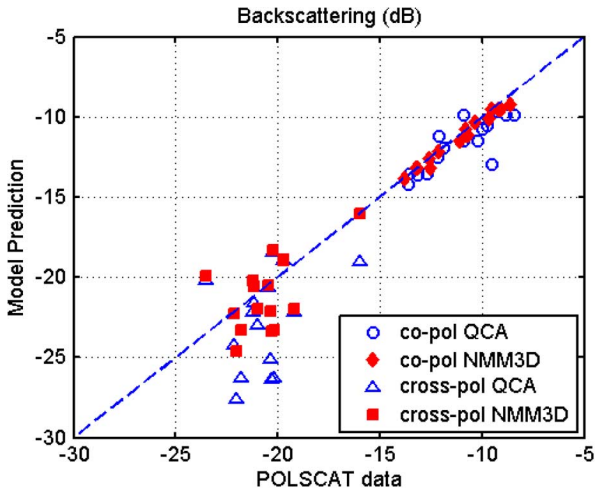

Fig. 10. Comparison Kuparuk River POLSCAT data with NMM3D/DMRT and QCA/DMRT simulation.

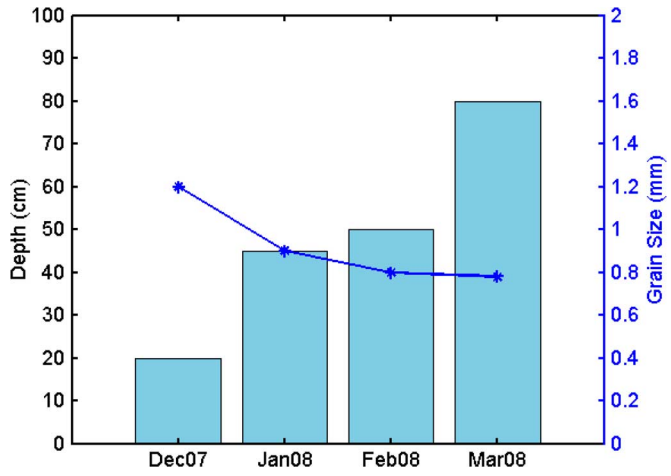

Fig. 12. Snow profile at Lake Catamount.

In Fig. 9, we show the Intensive Study Area (ISA) measurements of the snow depth. The x axis represents different places of ground measurement samples. The snow depth of the Kuparuk River ranges from 15–30 cm. The depth hoar is reported in the Alaska area, where the grain size is around 1–3 mm. In our model, the maximum grain size used is up to 1.5 mm. Both QCA/DMRT and NMM3D/DMRT were used to predict the backscattering coefficients. In Fig. 10, we show the error plot between the model predictions and the field measurements. For co-polarization, both QCA/DMRT and NMM3D/DMRT agree with the experiment data. For cross-polarization, the QCA/DMRT is below the measurements in some of the places where the snow densities are large. On the other hand NMM3D/DMRT yields good agreements for both co-polarization and cross-polarization backscattering coefficients.

B. Colorado Region

In the Colorado region, there were three intense observation periods completed in December 2006 (IOP1), January 2007 (IOP2), and February (IOP3). Unlike the Alaska region, the aircraft measurements in Colorado consisted of a variety of features, including coniferous and deciduous forest, sagebrush, pasture fields, and lake area.

In this paper, we make model comparisons with data from the Lake Catamount site. In this site, there is no vegetation effect. The data from POLSCAT show that the backscatter response increased significantly from December with data results from -44 dB to about -10 dB for the co-polarization backscattering coefficients. This means the lake has already frozen and the snow scattering dominates the radar response.

In Fig. 11, we show the changes in the backscattering coefficients during the 07–08 winter. Fig. 12 gives the corresponding snow depth and grain sizes as computed by the hydrology VIC model. We apply the NMM3D/DMRT model for this area. According to the results shown in Fig. 11 and Fig. 13, the NMM3D/DMRT model results show good agreements with POLSCAT data.

Another test field is from CLPX I snowpit in Fook Creek. We assume that the snow profiles from the ISA ground measurements vary little from pit to pit in Fool Creek, and POLSCAT observations vary little over different footprints. We apply the NMM3D/DMRT model using the ground measurements for Fool Creek snow pit 6. The average snow depth, snow

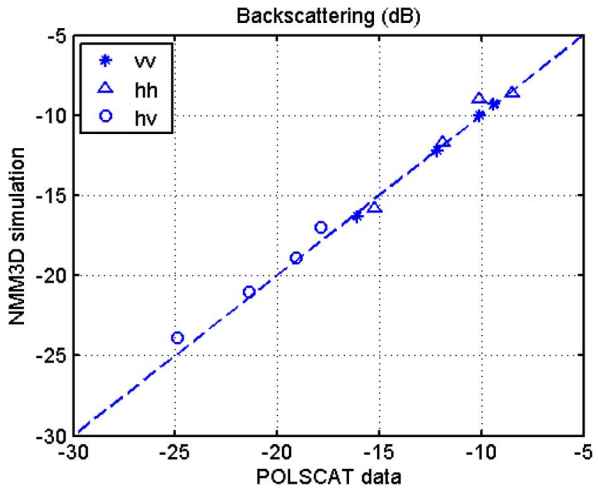

Fig. 13. Backscattering validation scatterplot at Lake Catamount.

TABLE I
BACKSCATTERING COEFFICIENT OBSERVATION AND MODEL SIMULATION

Channel	VV (dB)	HH (dB)	VH (dB)	HV (dB)
POLSCAT	-10.72	-10.81	-18.24	-17.86
QCA/DMRT	-10.28	-9.67	-21.94	-21.94
NMM3D/DMRT	-11.07	-10.77	-17.6	-17.6

density, and grain size of ground measurements are used. The POLSCAT observations, the NMM3D/DMRT model results and the QCA/DMRT model results are shown in Table I. The tabulated comparisons show that the NMM3D/DMRT model results agree with the POLSCAT observations.

V. CONCLUSION

To better understand the microwave interactions with terrestrial snow, we developed the physical forward NMM3D/DMRT model in this paper. The model is applicable for both active and passive microwave remote sensing of snow. The NMM3D was previously used to calculate the phase matrices and extinction coefficients. In this paper, it is combined with the DMRT equations. The predictions from hydrology VIC were used as the inputs for NMM3D/DMRT in the Colorado lake region. We also make model comparisons with CLPX II datasets in the Alaska region using the ground measurements. The NMM3D/DMRT yields good agreements with measurement data for cross-polarization backscattering as well as for co-polarization backscattering.

ACKNOWLEDGMENT

The author would like to thank the anonymous reviewers for their helpful and insightful comments.

REFERENCES

[1] L. Tsang, J. A. Kong, and K. H. Ding, *Scattering of Electromagnetic Waves, Vol 1. Theory and Applications*. Hoboken, NJ: Wiley-Interscience, 2000, pp. 170–171.

[2] H. Rott, S. Yueh, D. W. Cline, C. Duguay, R. Essery, C. Haas, F. Hélière, M. Kern, G. Macelloni, E. Malnes, T. Nagler, J. Pulliainen, H. Rebhan, and A. Thompson, "Cold regions hydrology high-resolution observatory for snow and cold land processes," *Proc. IEEE*, vol. 98, no. 5, pp. 752–765, May 2010.

[3] L. Tsang and J. A. Kong, *Scattering of Electromagnetic Waves, Vol. 3: Advanced Topics*. Hoboken, NJ: Wiley-Interscience, 2001, pp. 197–232.

[4] D. Liang, X. Xu, L. Tsang, K. M. Andreadis, and E. G. Josberger, "Multi-layer effects in passive microwave remote sensing of dry snow using Dense Media Radiative Transfer Theory (DMRT) based on quasi-crystalline," *IEEE Trans. Geosci. Remote Sens.*, no. 11, pp. 3663–3671, Nov. 2008.

[5] K. H. Ding, L. Tsang, and S. E. Shih, "Monte Carlo simulation of particle positions for densely packed multi-species sticky particles," *Microw. Opt. Technol. Lett.*, vol. 30, pp. 187–192, 2001.

[6] K. K. Tse, L. Tsang, C. H. Chan, K. H. Ding, and K. W. Leung, "Multiple scattering of waves by dense random distribution of sticky particles for applications in microwave scattering by terrestrial snow," *Radio Science*, vol. 42, Sep. 2007.

[7] L. Tsang, C. T. Chen, A. T. C. Chang, J. Guo, and K. H. Ding, "Dense media radiative transfer theory based on quasi-crystalline approximation with applications to passive microwave remote sensing on snow," *Radio Science*, vol. 35, no. 3, pp. 731–749, 2000.

[8] S. Yueh, D. Cline, and K. Elder, "Airborne Ku-band polarimetric radar remote sensing of terrestrial snow cover," in *Radar Conf.*, May 2008.

[9] K. M. Andreadis, D. Liang, L. Tsang, D. P. Lettenmaier, and E. G. Josberger, "Characterization of errors in a coupled snow hydrology-microwave emission model," *J. Hydrometeorol.*, vol. 9, no. 1, pp. 149–164, 2008.

[10] W. H. Stiles and F. T. Ulaby, "The active and passive microwave response to snow parameters 2. Water equivalent of dry snow," *J. Geophys. Res.*, vol. 85, no. C2, pp. 1045–1049, Feb. 1980.

[11] J. R. Kendra, K. Sarabandi, and F. T. Ulaby, "Radar measurement of snow: Experiment and analysis," *IEEE Trans. Geosci. Remote Sens.*, vol. 36, no. 3, pp. 864–879, May 1998.

[12] L. Tsang, J. A. Kong, and R. Shin, *Theory of Microwave Remote Sensing*. New York: Wiley, 1985.

[13] L. Tsang, J. Pan, D. Liang, Z. X. Li, D. Cline, and Y. H. Tan, "Modeling active microwave remote sensing of snow using dense media radiative transfer (DMRT) theory with multiple scattering effects," *IEEE Trans. Geosci. Remote Sens.*, vol. 45, no. 4, pp. 990–1004, Apr. 2007.

[14] L. Tsang, J. A. Kong, K. H. Ding, and C. O. Ao, *Scattering of Electromagnetic Waves, Vol 2. Numerical Simulations*. Hoboken, NJ: Wiley-Interscience, 2001.

[15] L. Tsang, M. C. Kubacsi, and J. A. Kong, "Radiative transfer theory for active remote sensing of a layer of ellipsoidal scatterers," *Radio Science*, vol. 16, no. 3, pp. 321–329, May–June 1981.

[16] C. T. Chen, L. Tsang, J. Guo, A. T. C. Chang, and K. H. Ding, "Frequency dependence of scattering and extinction of dense media based on three-dimensional simulations of Maxwell's equations with applications to snow," *IEEE Trans. Geosci. Remote Sens.*, vol. 41, no. 8, pp. 1844–1852, Aug. 2003.

[17] M. Hallikainen, F. Ulaby, and T. Deventer, "Extinction behavior of dry snow in the 18- to 90-GHz range," *IEEE Trans. Geosci. Remote Sens.*, vol. 25, pp. 737–745, 1987.

[18] X. Liang, D. P. Lettenmaier, E. F. Wood, and S. J. Burges, "A simple hydrologically based model of land surface water and energy fluxes for general circulation models," *J. Geophys. Res.*, vol. 99, pp. 14 415–14 428, 1994.

[19] K. Cherkauer and D. P. Lettenmaier, "Simulation of spatial variability in snow and frozen soil," *J. Geophys. Res.*, vol. 108, p. 8858, 2003, DOI: 10.1029/2003JD003575.

[20] K. M. Andreadis, P. Storck, and D. P. Lettenmaier, "Modeling snow accumulation and ablation processes in forested environments," *Water Resource Res.*, vol. 45, p. W05429, 2009, DOI: 10.1029/2008WR007042.

[21] C. Daly, R. P. Neilson, and D. L. Phillips, "A statistical-topographic model for mapping climatological precipitation over mountainous terrain," *J. Appl. Meteorol.*, vol. 33, pp. 140–158, 1994.

[22] E. P. Maurer, A. W. Wood, J. C. Adam, D. P. Lettenmaier, and B. Nijssen, "A long-term hydrologically based dataset of land surface fluxes and states for the conterminous United States," *J. Climate*, vol. 15, pp. 3237–3251, 2002.

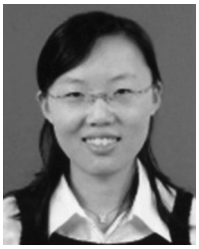

Xiaolan Xu (S'09) received the B.Eng. degree from Zhejiang University, Hangzhou, China, and the M.S. degree in electrical engineering from the University of Washington, Seattle. She is now working toward the Ph.D degree in electrical engineering at the University of Washington, Seattle.

She is now a research assistant in the Laboratory of Application and Computations in Electromagnetics and Optics. Her research interests include theoretical and numerical studies in random media and application in microwave remote sensing of environment.

Ding Liang received the B.Eng. degree from Wuhan University, Wuhan, China, and the M.S. and Ph.D. degrees in electrical engineering from the University of Washington, Seattle.

Leung Tsang (S'73-M'75-SM'85–F'90) received the B.S., M.S., and Ph.D. degrees from the Massachusetts Institute of Technology (MIT), Cambridge.

He is currently a Professor and the Chairman for Education with the Department of Electrical Engineering, University of Washington, Seattle, where he has been teaching since 1983. Between 2001 and 2004, while on leave, he was the Chair Professor and the Assistant Head with the Department of Electronic Engineering, City University of Hong Kong, Kowloon. His current research interests include remote sensing and geoscience applications, multiple scattering of waves, signal integrity, computational electromagnetics, and wireless communications.

Konstantinos M. Andreadis received the Engineering Diploma in environmental engineering from the Technical University of Crete, Chania, Greece, and the M.Sc.E. and Ph.D. degrees in civil and environmental engineering from the University of Washington, Seattle.

Edward G. Josberger received the B.S. degree in 1970 from New York University and the Ph.D. in 1979 from the University of Washington, Seattle.

He is currently leader of the USGS Ice and Climate Project, which measures the response of glaciers in the Pacific Northwest and Alaska to current global warming trends, using in situ and satellite observations. His research interests focus on remote sensing of the cryosphere. He collaborates with the University of Washington, NASA and the French Space Agency on deriving algorithms to extract snow depth information from satellite passive microwave observations.

Dennis P. Lettenmaier , photograph and biography not available at the time of publication.

Donald W. Cline , photograph and biography not available at the time of publication.

Simon H. Yueh received the Ph.D. degree in electrical engineering in January 1991 from the Massachusetts Institute of Technology, Cambridge.

He was a postdoctoral research associate at the Massachusetts Institute of Technology from February to August 1991. In September 1991, he joined the Radar Science and Engineering Section at the Jet Propulsion Laboratory (JPL), and worked as a radar system engineer for the SIR-C, NSCAT and SeaWinds missions. He was the supervisor of radar system engineering and algorithm development group from 2002-2007. He was the deputy manager of Climate, Oceans and Solid Earth section from 2007-2009, and became the section manager since early 2009. He led the Aquarius instrument team for a successful National Aeronautics and Space Administration (NASA) Earth System Science Pathfinder mission proposal, and has been serving as the Aquarius instrument scientist. He has been the Principal/Co-Investigator of numerous research projects, including the polarimetric wind radiometer research; airborne scatterometer project for hurricane wind measurements; Passive/Active L-band Sensor (PALS) project; NASA Instrument Incubator Project for a mission concept using a large mesh-deployable antenna for soil moisture and ocean salinity sensing; the airborne polarimetric radar (POLSCAT) for ocean wind velocity measurements; the POLSCAT/Cold Land Processes Experiment (CLPX) in 2002-2004; the Advanced Component Technology lightweight dual-frequency antenna feed project; the POLSCAT experiments for CLPX-2 in 2006-2008 and for CLPX-3 in 2009-2010; and the Aquarius PALS High Wind Campaign in 2009. He is leading the development of Snow and Cold Land Processes mission concept at JPL. He has authored four book chapters and published more than 150 publications and presentations.

Dr. Yueh received the 2009 IEEE GRSS Transactions Prize Paper award, 2002 IEEE GRSS Transaction Prize Paper award, the 2000 Best Paper Award in the IEEE International Geoscience and Remote Symposium 2000, and the 1995 IEEE GRSS Transaction Prize Paper award for a paper on polarimetric radiometry. He received the JPL Lew Allen Award in 1998 and Ed Stone Award in 2003. He is an associate editor of IEEE TRANSACTIONS ON GEOSCIENCE AND REMOTE SENSING, and a Fellow of IEEE.